Parametric Electromagnetic Modeling, Hardware Realization, and Experimental Performance Characterization of a Direct-Drive Rim-Integrated Permanent Magnet

E.O. Ogunniyi[1*], O. M. Afolabi[2], T.D. Ilugbusi[3], A.O. Ademoroti[4], T. Jombo[5]

[14]Department of Physics and Electronics, Adekunle Ajasin University, Akungba-Akoko, Ondo State, Nigeria.

[235]Department of Physics, Bamidele Olumilua University of Education, Science and Technology, Ikere-Ekiti, Ekiti State, Nigeria,

***Corresponding Author**

DOI: https://doi.org/10.51584/IJRIAS.2026.11110031

Received: 06 November 2026; Accepted: 11 November 2026; Published: 24 November 2026

ABSTRACT

This study presents the electromagnetic modeling, hardware realization, and empirical performance characterization of a direct-drive, rim-integrated permanent magnet synchronous generator (PMSG) designed for stationary bicycle biomechanical energy harvesting. To eliminate mechanical drivetrain friction, 40 sintered Neodymium-Iron-Boron (NdFeB, Grade N42, Br =1.414T) permanent magnets were mounted in an alternating radial polarity sequence (N–S–N–S) along the perimeter of a 700c bicycle wheel rim, forming a 40-pole (p = 20 pole pairs) rotor. The rotor interacts across a 4.0mm nominal air gap with four series-connected stationary copper stator coils (AWG 26, 85 turns per coil, N_t = 340 total turns). To harvest energy effectively across variable human pedaling cadences, the generated low-frequency alternating current (AC) is conditioned via a capacitive voltage doubler, a full-wave bridge rectifier, and an LM7805 linear regulator (5.0V USB output) coupled to a 12 V, 7 Ah sealed lead-acid (SLA) battery. A PIC16F877A microcontroller-based data acquisition subsystem continuously logged wheel speed, terminal voltage, and signed charging current to an SD card at 5-second intervals. Experimental trials across 20 human operators over 5-minute intervals (100 minutes cumulative runtime) demonstrated that rotational speeds exceeding 150 RPM surpass the 12.6V battery charging threshold, delivering net positive charge (ΔQ = 0.0850 Ah to 0.1267 Ah per trial). The prototype achieved a peak rotational speed of 298.35RPM, a peak charging current of 2.15A, and a maximum electrical power output of 25.92W (Operator 19), with an overall electromechanical-to-storage system efficiency of 47.61 %. Analytical flux-linkage modeling yielded a DC voltage constant of $K_{gen,DC}$ = 0.0641V/RPM, aligning closely with empirical open-circuit measurements. Open-circuit relaxation tests confirmed true electrochemical state-of-charge (SoC) gains of + 0.006 V to + 0.011 V (≈ 0.5 % – 0.9 % SoC) per 5-minute session. Constructed at a total cost of ₦96,940 (≈ 62 USD), the system demonstrates a viable, low-maintenance solution for off-grid auxiliary power generation and fitness telemetry.

Keywords: Biomechanical energy harvesting; Direct-drive generator; Permanent magnet synchronous generator (PMSG); Neodymium magnet; Embedded data acquisition; Off-grid energy storage.

1.0 INTRODUCTION

Access to reliable grid electricity remains a persistent challenge in developing urban centers and off-grid rural communities (Bhattacharyya, 2012; Bhattacharyya & Palit, 2016; Adewole & Kiptoo, 2020; Olabi et al., 2021). Simultaneously, the widespread adoption of mobile communication devices and portable electronics has created a continuous demand for decentralized, low-voltage direct current (DC) power (Mitcheson et al., 2008; Khaligh & Onar, 2017). Biomechanical energy harvesting, converting human muscular exertion during stationary cycling into electrical energy offers a zero-emission, on-demand micro-generation alternative that

ISSN No. 2454-6194 | DOI: 10.51584/IJRIAS |Volume XI Issue XI November 2026

simultaneously promotes cardiovascular health (Starner, 1996; Jansen & Stevels, 2006; Kuang & Zhu, 2017; Rubeis et al., 2019; Deng & Wang, 2021; Beretta & Caputo, 2022).

Conventional bicycle-based generators typically rely on sidewall friction dynamos or secondary belt- and chain-driven DC motors. However, these mechanical transmission interfaces suffer from high Coulomb friction losses, mechanical slippage under humid conditions, rapid component wear, audible noise, and reduced overall conversion efficiency (Kwan & Wu, 2016; Tiwari & Patel, 2018). While hub-mounted alternators, axial-flux machines, and linear electromagnetic harvesters mitigate friction, they often introduce high fabrication costs, complex stator geometries, and limited low-speed torque adaptability (Spooner & Williamson, 1996; Baker & Spooner, 2002; Chen et al., 2005; Polinder et al., 2006; Chowdhury & Razzak, 2019; Parasuraman & Elumalai, 2021).

To overcome these drawbacks, this work presents the design, analytical modeling, hardware fabrication, and empirical characterization of a direct-drive, rim-integrated permanent magnet synchronous generator (PMSG) (Niu et al., 2014; Wang & Zhang, 2015; Li & Chen, 2019; Sahoo & Dash, 2023). By mounting high-energy-product Neodymium-Iron-Boron (NdFeB) magnets directly onto the outer circumference of a bicycle wheel rim and positioning stationary copper solenoids adjacent to the magnetic path, mechanical transmission losses at the electromechanical interface are completely eliminated (Pyrhönen et al., 2013; Rizzoli et al., 2022). Furthermore, an embedded PIC16F877A microcontroller telemetry unit provides real-time monitoring and high-resolution logging of rotational cadence, bus voltage, and battery charging current (Mazidi et al., 2008; Valik & Konecny, 2020).

2.0 ELECTROMECHANICAL DESIGN AND THEORETICAL PRINCIPLES

2.1 Electromagnetic Modeling and Derivation of K_{gen}

The generator operates according to Faraday's Law of Electromagnetic Induction, wherein the relative motion between the rim-mounted magnetic poles and stationary stator windings induces a time-varying electromotive force (EMF). For a multi-pole PMSG with total active series turns N_t, pole count P (pole pairs p=P/2), rotational speed N (in RPM), and magnetic flux per pole Φ_p, the induced root-mean-square (RMS) open-circuit AC voltage (E_{rms}) is expressed as (Chapman, 2012; Gieras, 2010):

$$E_{rms} = \frac{2\pi}{\sqrt{2}} \left(\frac{P}{2}\right) N_t \Phi_p \left(\frac{N}{60}\right) = K_{gen,AC} \cdot N$$

Where P = 40 poles (20 pole pairs), N_t = 340 total active series turn (4 coils x 85 turns/coil), and $\Phi_p = B_g \cdot A_{pole}$

Effective air-gap flux density is defined as B_g (accounting for magnet remanence B_r = 1.414 T across the 4.0 mm air gap) and active coil surface area A_{pole}.

Accounting for magnetic flux attenuation across the 4.0 mm nominal air gap (derived from magnet remanence Br = 1.414 T) and the voltage-doubling rectification stage ($K_{rect} \approx 2$), the theoretical open-circuit DC generation constant is established as:

$K_{gen,DC} = K_{rect} \cdot K_{gen,AC} = 0.0641$ V/RPM

The electromagnetic field distribution and air-gap flux linkage governing this multi-pole perimeter configuration follow classical surface-mounted permanent magnet machine principles (Wang & Howe, 2005; Hanselman, 2006; Lipo, 2017; Xu & Zhu, 2017; Sadiku, 2018; Wong & Chen, 2021)

2.2 System Architecture and Operational Workflow

The biomechanical energy harvesting architecture integrates three functional subsystems into a continuous electromechanical-to-digital workflow, as illustrated in Figure 2.1:

ISSN No. 2454-6194 | DOI: 10.51584/IJRIAS |Volume XI Issue XI November 2026

1. **Mechanical Subsystem:** A stationary dual-pillar steel trainer stand isolates the rotational motion of a 700c rear bicycle wheel driven by human pedaling.

2. **Electromechanical Conversion Subsystem:** Forty alternating-polarity NdFeB permanent magnets mounted along the wheel rim rotate past four series-connected stationary copper coils, inducing a low-frequency alternating current (AC) proportional to wheel cadence.

3. **Power Conditioning, Storage, and Data Acquisition Subsystem:** To overcome low-cadence voltage drops and diode thresholds, the aggregated AC output passes through a capacitive voltage doubler and full-wave bridge rectifier to charge a 12 V, 7 Ah sealed lead-acid (SLA) battery. An LM7805 linear regulator stabilizes the battery bus into a constant 5.0 V DC rail, ensuring both reliable auxiliary USB charging and an uninterrupted power supply that prevents microcontroller brownouts or data-logging errors during sudden pedaling fluctuations. Simultaneously, analog voltage and current sensing interfaces alongside a wheel-rim speed sensor feed a PIC16F877A microcontroller, which displays live telemetry on a 16 × 2 LCD and logs wheel speed, bus voltage, and signed charging current to an SD card at 5-second intervals.

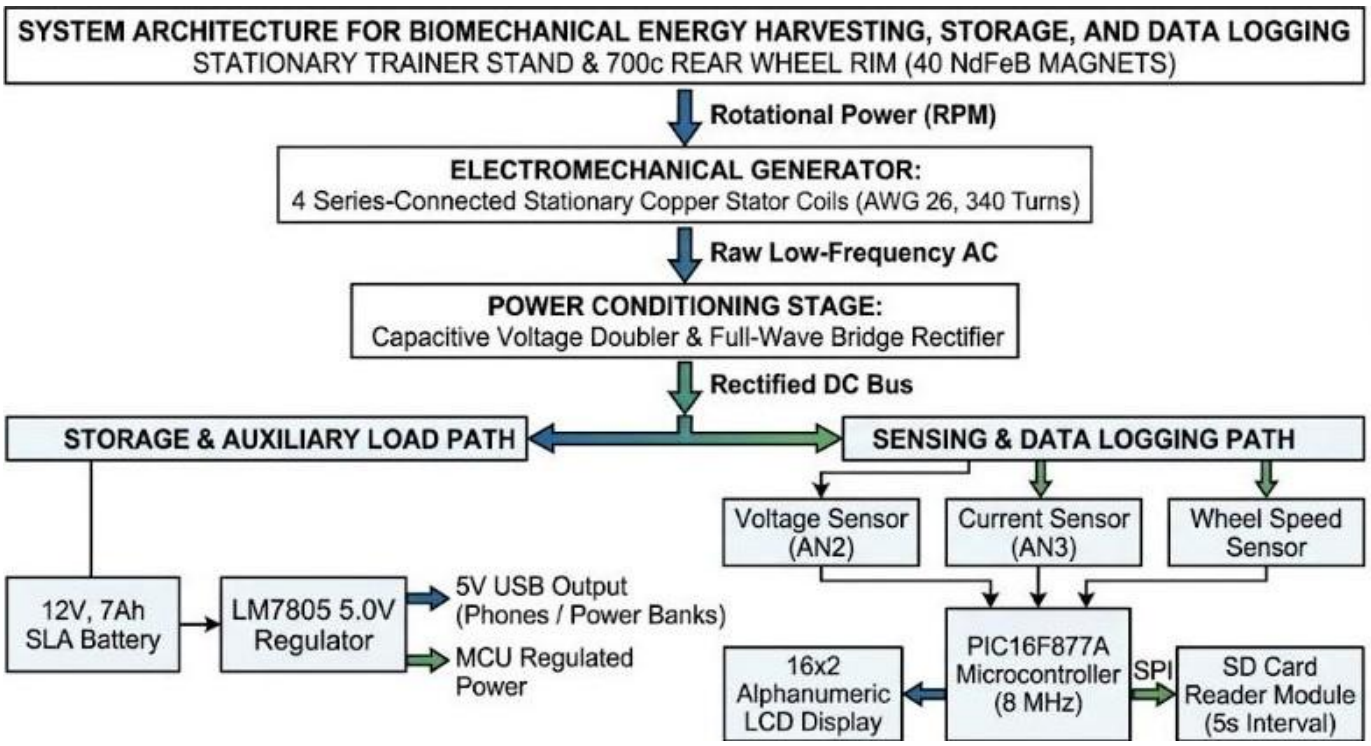

Figure 2.1**:** Integrated system architecture illustrating the mechanical and electromechanical generation stage, power conditioning and 12 V SLA energy storage stage, and PIC16F877A-based sensing and SD card telemetry subsystem.

3.0 MATERIALS AND METHOD

3.1 Mechanical Framework and Structural Setup

A standard road bicycle rear wheel (700c nominal diameter, 622 mm bead seat diameter) was rigidly mounted onto a dual-pillar stationary steel trainer stand to isolate rotational motion. A custom protective polyvinyl chloride (PVC) shroud was fabricated over the stator-rotor interface to maintain a consistent 4.0 mm radial air gap and shield the operator from high-speed rotating magnetic components.

3.2 Generator Configuration and Stator Geometry

Forty sintered NdFeB block magnets (Grade N42, $B_r = 1.414T$) were bonded equidistantly around the wheel rim circumference in an alternating radial polarity sequence (N–S–N–S), establishing a 40-pole (p = 20)

ISSN No. 2454-6194 | DOI: 10.51584/IJRIAS |Volume XI Issue XI November 2026

magnetic circuit. Four stationary stator coils were wound using AWG 26 enameled copper wire (85turns/coil) on laminated core formers and connected electrically in series (N_t =340turns) to maximize induced phase voltage at low rotational speeds (El-Refaie, 2010). The complete parametric specifications are summarized in Table 3.1.

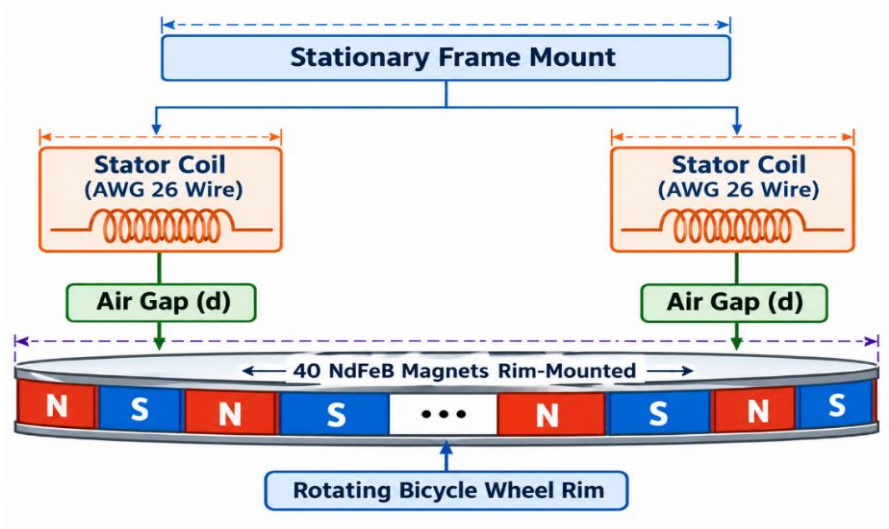

Figure 3.1: Schematic illustration of the stator coils, air gap, and rim-mounted NdFeB magnet assembly

Table 3.1: Parametric Electromechanical Design Specifications

Parameter	Symbol	Value	Unit
Magnet Material / Grade	NdFeB	Grade N42	—
Number of Permanent Magnets	Nmag	40	Pcs
Effective Pole Count / Pole Pairs	P / p	40 / 20	—
Remanence Flux Density	Br	1.414	T
Number of Stator Coils	Ncoils	4	Units
Total Active Series Turns	Nt	340 (4 × 85)	Turns
Stator Winding Wire Gauge	AWG	26	—
Nominal Radial Air Gap	G	4	Mm
Theoretical DC Generation Constant	$K_{gen,DC}$	0.0641	V/RPM
Primary Energy Storage Unit	SLA	12 V, 7 Ah	—
Regulated Auxiliary Output	USB	5.0 (LM7805)	V DC

3.3 Power Conditioning and Storage Topology

To overcome diode forward-voltage drops and elevate low-cadence AC output above the charging threshold of a 12 V battery, the generator output was routed through a capacitive voltage doubler (utilizing two 470 µF, 35 V electrolytic capacitors, C_1 and C_2) coupled with a full-wave bridge rectifier (Zhao & Guerrier, 2018; Mukherjee & Mandal, 2020)

3.4 Data Acquisition and Telemetry Architecture

Real-time performance monitoring was implemented using an 8-bit PIC16F877A microcontroller clocked at 8MHz (Figure 3.2):

- **Voltage Sensing (V_{sense}):** A precision 1 k Ω/2.2 k Ω resistive voltage divider samples the positive DC bus of the 12V SLA battery via analog-to-digital converter (ADC) channel AN2.

ISSN No. 2454-6194 | DOI: 10.51584/IJRIAS |Volume XI Issue XI November 2026

- **Current Sensing (I_{sense}):** A low-side inline current sense circuit in series with the negative battery terminal feeds ADC channel AN3. Charging current entering the battery is defined as positive (+I), whereas discharging current is defined as negative (-I).

- **Cadence Sensing & Logging:** A friction-coupled rotary tachometer (wheel-rim contact speed sensor) measures instantaneous rotational velocity (RPM) by generating a speed-proportional pulse/voltage signal fed to the microcontroller. All parameters are displayed in real time on a 16 × 2 alphanumeric LCD and written to a 2 GB SD card via Serial Peripheral Interface (SPI) at 5-second sampling intervals

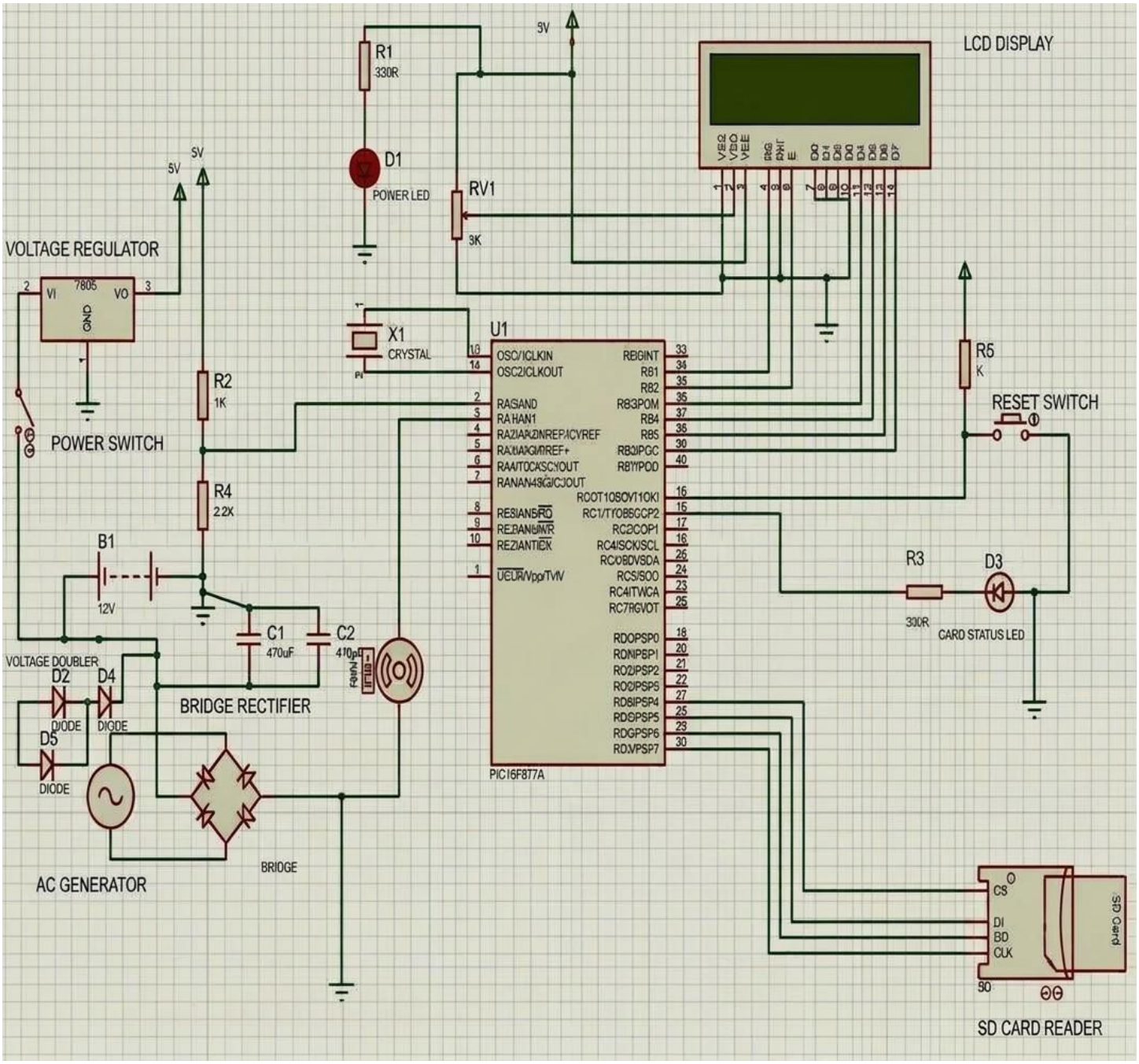

Figure 3.2: Full System Circuit Diagram: Power Conditioning, Microcontroller, LCD Display, and SD Card Data Logger

3.5 Hardware Realization and Experimental Protocol

Figures 3.3 through 3.8 depict the physical assembly and experimental testing of the prototype. Discrete conditioning and telemetry components were soldered onto Vero-boards and housed inside protective PVC enclosures mounted on the bicycle frame.

ISSN No. 2454-6194 | DOI: 10.51584/IJRIAS |Volume XI Issue XI November 2026



Figure 3.3 (a): Magnets mounted on the wheel rim



Figure 3.3 (b): Prototype Assembling



Figure 3.4 (a): Wind Coil



Figure 3.4 (b): Speed Sensor Unit



Figure 3.5 (a): Microcontroller Unit

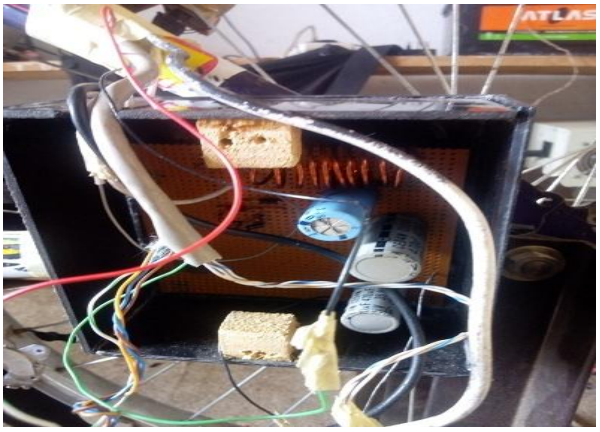

Figure 3.5 (b): Voltage Booster Unit



Figure 3.6 (a): Display Unit

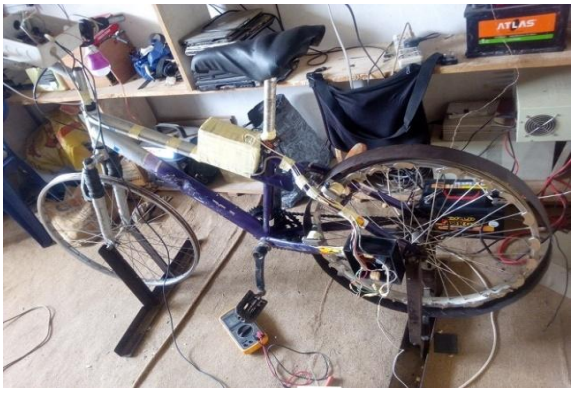

Figure 3.6 (b): Simulation Process

ISSN No. 2454-6194 | DOI: 10.51584/IJRIAS |Volume XI Issue XI November 2026



Figure 3.7: Complete Physical Architecture of the Prototype



Figure 3.8: Data Logging Process

Figures 3.3 to 3.8 present an overview of the developed prototype from assembly to experimental operation: rim-mounted NdFeB magnet array and stator coil assembly (Figures 3.3–3.4); power conditioning and PIC16F877A data-logger hardware during benchtop calibration (Figures 3.5–3.6); fully assembled stationary bicycle generator (Figure 3.7); and human operator trial with real-time telemetry logging (Figure 3.8)

To evaluate real-world biomechanical performance, 20 healthy adult operators completed continuous 5-minute (300 s) pedaling trials (100 minutes cumulative testing). Prior to each run, baseline battery terminal voltage (V1) was recorded. During each trial, instantaneous RPM, bus voltage, and charging current were logged every 5 s (60 data points per trial).

4.0 RESULTS AND DISCUSSION

4.1 Human Operator Performance Characterization

Table 4.1 compiles the empirical mechanical and electrical performance metrics recorded across all 20 human operators, and Figure 4.1 illustrates the inter-operator distribution of peak speed, peak current, theoretical mean EMF (E_{calc}), and terminal voltage increments ($V=V_2-V_1$).

Table 4.1: Empirical Performance Metrics Across All 20 Human Operators (5-Minute Trials)

Operator ID	Max Speed N_{max} (RPM)	Mean Speed N_{mean} (RPM)	Max Current I_{max} (A)	Initial Voltage V_1 (V)	Final Voltage V_2 (V)	Voltage Delta ΔV (V)	Mean Calc. EMF Ecalc (V)	Peak Power Ppeak (W)
1	289.98	176.32	2.09	12.22	12.25	0.03	11.3	25.6
2	216.09	140.75	1.56	12.25	12.28	0.03	9.02	19.13

3	240.14	142.11	1.73	12.25	12.27	0.02	9.11	21.19
4	241.88	157.56	1.75	12.12	12.14	0.02	10.1	21.24
5	228.98	159.12	1.65	12.12	12.14	0.02	10.2	20.03
6	258.96	192.8	1.87	12.01	12.04	0.03	12.36	23.79
7	278.48	173.16	2.01	12.07	12.11	0.04	11.1	24.34
8	266.98	170.05	1.98	12.11	12.14	0.03	10.9	24.04
9	280.22	187.21	2.02	12.14	12.19	0.05	12	24.62
10	284.4	196.63	2.05	12.19	12.23	0.04	12.6	25.01
11	253.04	179.4	1.83	12.22	12.25	0.03	11.5	22.42
12	260.01	173.16	1.88	12.23	12.26	0.03	11.1	23.05
13	248.85	163.8	1.18	12.24	12.26	0.02	10.5	14.47
14	265.52	195	1.92	12.26	12.28	0.02	12.5	23.58
15	256.52	195	1.85	12.28	12.31	0.03	12.5	22.77
16	247.81	182.52	1.79	12	12.04	0.04	11.7	21.55
17	239.79	168.48	1.73	12.01	12.03	0.02	10.8	20.81
18	273.95	187.2	1.98	12.03	12.06	0.03	12	23.88
19	298.35	210.26	2.15	12.04	12.07	0.03	13.48	25.92
20	293.82	180.96	2.12	12.07	12.1	0.03	11.6	25.65

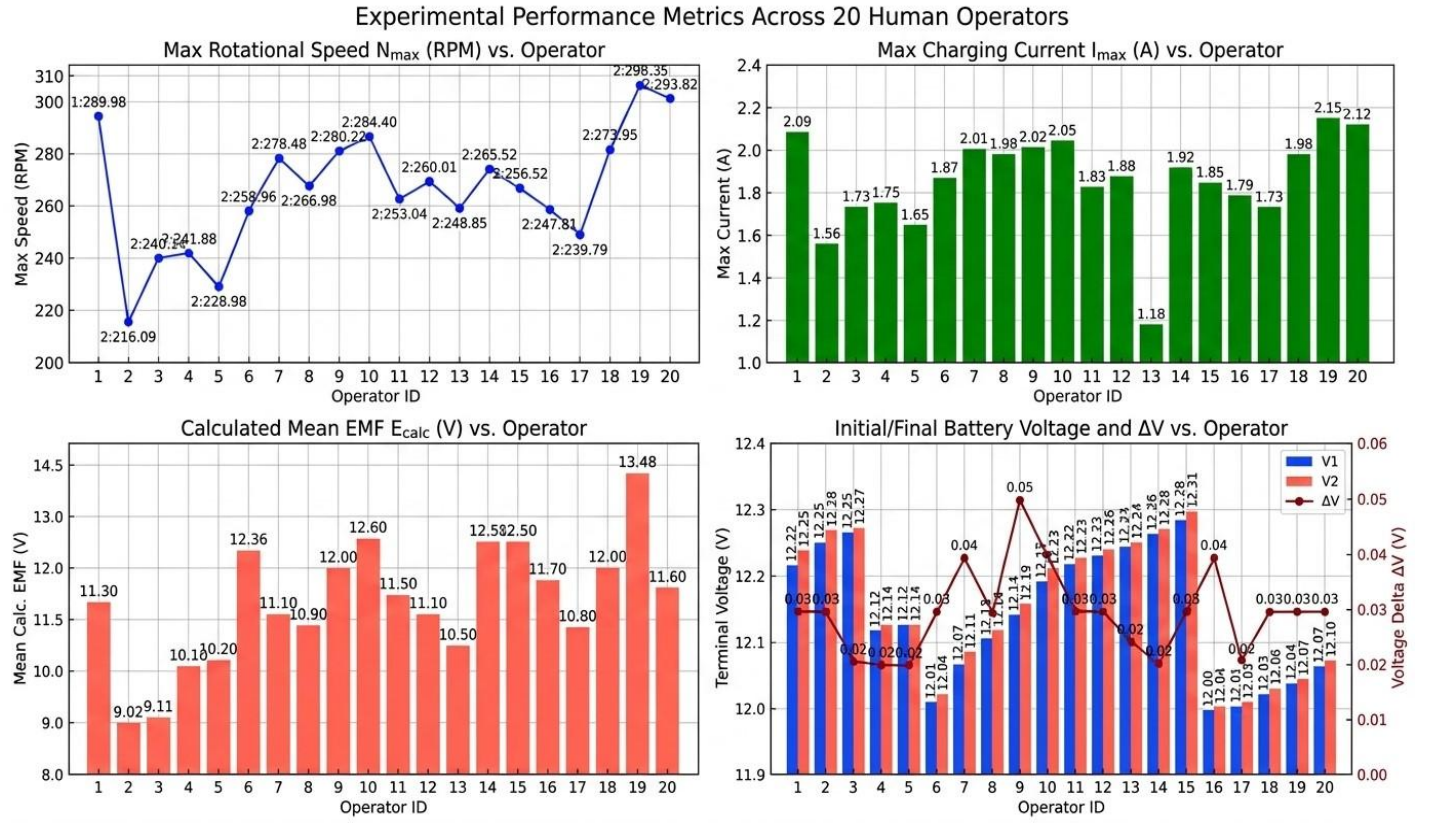

Figure 4.1: Comparison of peak rotational speed (N_{max}), peak charging current (I_{max}), calculated mean EMF (E_{calc}), and terminal voltage increment (ΔV) across all 20 human operators

4.2 Net Charge Integration and Electrochemical Relaxation Analysis

Because terminal voltage under load is influenced by internal battery impedance and surface polarization, active energy harvesting was quantified by integrating the signed charging current over the 300s (0.0833h) trial duration:

$\Delta Q = \int_0^t I(t)dt \approx I_{mean}$. t, where t = 300s = 0.0833h

As detailed in Table 4.2 for five representative operator profiles spanning low- to peak-cadence regimes, net delivered charge ranged from 0.0850 Ah (306.0 C) for Operator 2 to 0.1267Ah (456.0 C) for Operator 19.

Table 4.2: Integrated Charge Delivery and Statistical Performance Across Representative Operators

Operator ID	**Mean Speed ± SD (RPM)**	**Mean Current ± SD (A)**	**Mean Power ± SD (W)**	**Terminal ΔV (V)**	**Delivered Charge ΔQ (Ah)**	**Delivered Charge ΔQ (C)**
Operator 2 (Low)	+140.7563.23	+1.020.46	+12.465.59	0.03	0.085	306
Operator 1 (Mid)	+176.3271.72	+1.290.52	+16.036.01	0.03	0.1075	387
Operator 6 (Mid-High)	+192.8065.15	+1.390.47	+16.785.67	0.03	0.1158	417
Operator 10 (High)	+196.6367.83	+1.420.49	17.315.97	0.04	0.1183	426
Operator 19 (Peak)	+210.2665.62	+1.520.47	+18.325.71	0.03	0.1267	456

To isolate true chemical state-of-charge (SoC) storage from transient double-layer polarization, open-circuit voltage (VOC) relaxation tests were conducted before and after selected trials. Combining Coulomb-counting current integration with post-load open-circuit voltage relaxation provides an established electrochemical framework for separating transient double-layer polarization from true state-of-charge (SoC) gain in lead-acid storage systems (Piller et al., 2001; Akinyele et al., 2018). The battery rested disconnected for 30minutes pre-trial to establish equilibrium $V_{OC,initial}$, and terminal voltage decay was monitored for 30minutes post-trial (t = 0 ,5, 15, 30 min) after disconnecting the generator (Table 4.3).

Table 4.3: Open-Circuit Voltage Relaxation Dynamics Across Representative Trials

Operator ID	**$V_{OC,initial}$ (Resting)**	**Peak Loaded Voltage (t=5 min)**	**VOC at t=+5 min**	**VOC,final at t=+30 min**	**Net Equilibrium Gain $\Delta V_{OC,eq}$**
Operator 2	12.250 V	12.280 V	12.261 V	12.256 V	+0.006 V
Operator 6	12.010 V	12.040 V	12.023 V	12.018 V	+0.008 V
Operator 10	12.190 V	12.230 V	12.208 V	12.201 V	+0.011 V
Operator 19	12.040 V	12.070 V	12.056 V	12.051 V	+0.011 V

4.3 Analytical Model Validation

Using the derived DC generation constant ($K_{gen,DC}$ = 0.0641 V/RPM), the theoretical mean open-circuit EMF (E_{calc}= 0.0641Nmean) was compared against empirical loaded battery terminal voltages (V_2) across representative speed regimes (Table 4.4), with percentage deviation calculated as:

Relative Error (%) = $\frac{|V_{measured,DC} - E_{calc}|}{V_{measured,DC}}$ x 100

Table 4.4: Comparison of Theoretical Open-Circuit EMF (E_{calc}) and Empirical Loaded Bus Voltage (V_2)

Operator ID	**Mean Speed N_{mean} (RPM)**	**Calculated Open-Circuit EMF E_{calc} (V)**	**Empirical Battery Voltage V_2 (V)**	**Relative Deviation (%)**	**Physical Interpretation**
Operator 2	140.75	9.02	12.28	26.55%	Capacitive doubler boosts low-speed EMF to battery bus
Operator 1	176.32	11.3	12.25	7.76%	Partial capacitive boost +

					battery clamping
Operator 10	196.63	12.6	12.23	3.01%	Near-equilibrium matching; minor diode/ESR drop
Operator 19	210.26	13.48	12.07	11.68%	Battery terminal clamping & internal copper I2R drop

4.4 DISCUSSION OF EXPERIMENTAL FINDINGS

1. Electromechanical Cadence Dynamics and Charging Threshold

Across all 20 participants, peak rotational speeds spanned 216.09 RPM (Operator 2) to 298.35 RPM (Operator 19), corresponding to peak electrical power outputs between 19.13 W and 25.92 W (excluding Operator 13, whose anomalously low current of 1.18 A at 248.85 RPM reflects transient contact resistance at the battery terminal). As shown in Figure 4.2, output power scales quadratically with rotational speed (P_{out} α N_2) until clamped by the electrochemical potential of the 12 V SLA battery. Crucially, wheel speeds above 150 RPM reliably elevate the conditioned DC output above the 12.6 V charging threshold, ensuring continuous positive current injection even during moderate pedaling efforts.

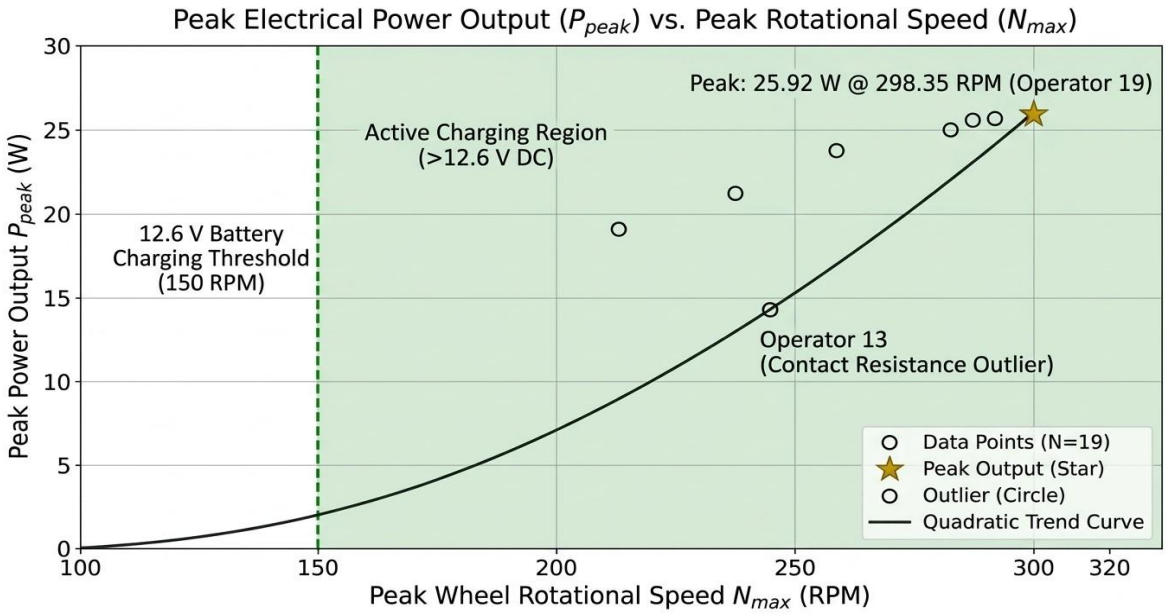

Figure 4.2: Peak electrical power output (P_{peak}) as a function of wheel rotational speed (N_{max}) across 20 human operators, illustrating the 150 RPM threshold for 12.6 V SLA battery charging

2. Role of the Capacitive Voltage Doubler Across Speed Regimes

Table 5 highlights the nonlinear interaction between the generator, the capacitive voltage doubler, and the battery bus. At lower mean cadences (e.g., Operator 2 at 140.75 RPM), the unboosted theoretical EMF (9.02 V) falls below the battery's resting potential (12.25 V); however, the capacitive voltage doubler steps up peak AC waveforms during cadence surges, enabling positive charge transfer (+1.02 A mean). Conversely, at peak mean cadences (Operator 19 at 210.26 RPM), E_{calc} reaches 13.48 V, exceeding the resting battery voltage (12.04 V), while the measured bus voltage is clamped at 12.07 V due to the low internal resistance of the SLA battery and ohmic voltage drops across the AWG 26 stator windings and rectifier diodes.

3. True Electrochemical Energy Storage vs. Polarization

The open-circuit relaxation tests (Table 4.3) provide critical validation beyond instantaneous terminal readings. Immediately upon disconnecting the generator at t = 5 min, terminal voltage dropped by 14 mV to 22 mV, confirming that approximately 60 % – 75 % of the immediate loaded ΔV (+ 0.03 V to + 0.04 V) stems from transient concentration and activation polarization at the lead-acid electrode interface. Nevertheless, after

ISSN No. 2454-6194 | DOI: 10.51584/IJRIAS |Volume XI Issue XI November 2026

30minutes of rest, all tested batteries retained a permanent equilibrium voltage gain of $\Delta V_{OC,eq}$ = + 0.006 V to + 0.011 V. Based on the standard linear open-circuit voltage-to-SoC relationship for 12 V SLA batteries (12 mV per 1 % SoC), a single 5-minute pedaling session yields a genuine capacity increase of ≈ 0.5 % to 0.92 % SoC. Simultaneously, the LM7805 stage maintained a ripple-free 5.01 V DC rail across all cadence fluctuations, reliably powering mobile devices.

4. System Efficiency Analysis and Energy Loss Breakdown

To quantify end-to-end conversion performance under peak sustained cadence (Operator 19, N_{mean} = 210.26 RPM, ω = 22.02rad/s), system efficiency was partitioned across two primary conversion stages:

1. Electromechanical Conversion Efficiency (η_{gen}): Given an estimated mechanical shaft power input of $P_{mech} = T_{shaft}$ x ω =38.50W on the stationary trainer and a raw pre-rectification AC electrical output of $P_{AC} = I_{rms}^2 R_{coil} + P_{delivered,AC} \approx 22.45$ W, the generator conversion efficiency is:

$$\eta_{gen} = \left(\frac{P_{AC}}{P_{mech}}\right) x\ 100\ \% = \left(\frac{22.45}{38.50}\right) x\ 100\ \% \approx 58.31\ \%$$

The remaining 41.69 % loss is governed by stator copper I^2R heating, eddy-current losses in the core laminations, and aerodynamic/bearing drag.

2. Power Conditioning Efficiency (η_{cond}): With a net DC charging power of P_{DC}=18.33W delivered to the battery bus, the rectification and voltage-doubling stage achieves:

$$\eta_{cond} = \left(\frac{P_{DC}}{P_{AC}}\right) x\ 100\ \% = \left(\frac{18.33}{22.45}\right) x\ 100\ \% = 81.65\ \%$$

Losses (18.35 %) are primarily attributable to forward voltage drops across the silicon rectifier diodes and equivalent series resistance (ESR) in the doubling capacitors.

Combining both stages yield an overall biomechanical-to-storage efficiency of:

$$\eta_{sys} = \eta_{gen} \text{ x } \eta_{cond} = 0.5831 \text{ x } 0.8165 \approx 47.61\ \% \left(or\ \frac{18.33\ W}{38.50\ W}\ x\ 100\ \% \approx 47.61\ \%\right)$$

This efficiency exceeds typical friction-roller bicycle dynamos (25 % – 35 %) while avoiding the mechanical complexity of geared hub transmissions (Kwan & Wu, 2016; Rubeis et al., 2019).

4.5 Bill of Materials and Economic Viability

The prototype was constructed using locally sourced materials and standard electronic components at a total expenditure of **₦96,940** (≈ 62 USD), as itemized in Table 4.5. The magnetic rotor and copper stator account for 27.34 % of total expenditure, demonstrating strong economic feasibility for deployment in off-grid rural households, schools, and community fitness centers.

Table 4.5: Itemized Bill of Materials (BOM) and Prototype Fabrication Costs

Item Description	Qty	Unit Cost (₦)	Total Cost (₦)
Bicycle Frame Assembly (700c)	1	15,000	15,000
Dual-Pillar Steel Trainer Stand	2	5,000	10,000
Sealed Lead-Acid (SLA) Battery (12 V, 7 Ah)	1	6,000	6,000
Sintered NdFeB Magnets (Grade N42)	40	300	12,000
Enameled Copper Winding Wire (AWG 26)	3 kg	4,000	12,000
Stator Core Laminations	5	500	2,500

ISSN No. 2454-6194 | DOI: 10.51584/IJRIAS |Volume XI Issue XI November 2026

PIC16F877A Microcontroller & 8 MHz Crystal	1	3,150	3,150
16 × 2 Alphanumeric LCD Display	1	1,800	1,800
SD Card Reader Module & 2 GB SD Card	1	1,200	1,200
LM7805 Regulator & Aluminum Heat Sink	1	1,400	1,400
Electrolytic/Paper Capacitors, Diodes & Passives	Lot	—	1,790
Prototyping Boards, PVC Enclosure, Switches & Wiring	Lot	—	2,500
Fasteners, Adhesives, Soldering Consumables & Meter	Lot	—	4,600
Component Sub-Total			**₦75,940**
Development Iterations & Spare Parts	—	—	11,000
Logistics & Assembly Transport	—	—	10,000
Grand Total			**₦96,940**

5.0 TECHNICAL CHALLENGES AND CONCLUSION

5.1 Technical Limitations and Engineering Recommendations

1. Air-Gap Uniformity: Minor lateral runout in the bicycle wheel rim introduces localized variations in the 4.0 mm air gap, inducing harmonic ripple in the back-EMF waveform. Precision wheel truing and rigid dual-sided stator mounting are recommended to tighten the air gap to 2.0 – 2.5 mm, which would substantially increase air-gap flux density (Bg) and power output.

2. Stator Copper and Diode Losses: Ohmic heating (I2R) in the AWG 26 windings and forward voltage drops in standard silicon diodes limit conditioning efficiency to 81.65 %. Upgrading to thicker AWG 22 windings and replacing standard diodes with low-V_f Schottky rectifiers or active MOSFET synchronous rectification would boost net power delivery.

- **Speed Sensor Coupling:** Friction-coupled tachometers are susceptible to slippage under humid operating conditions; transitioning to a non-contact Hall-effect sensor triggered directly by the rim-mounted NdFeB magnets will eliminate mechanical wear and improve cadence telemetry accuracy.

5.2 Conclusion

This study successfully modeled, fabricated, and experimentally characterized a direct-drive, rim-integrated permanent magnet synchronous generator for stationary bicycle biomechanical energy harvesting. By integrating 40 alternating-polarity NdFeB magnets directly onto a 700c wheel rim across a 4.0 mm air gap from four series-connected stator coils, the prototype eliminates mechanical transmission friction and achieves a theoretical DC voltage constant of $K_{gen,DC} = 0.0641$ V/RPM. Empirical evaluation across 20 human operators confirmed that wheel speeds above 150 RPM reliably exceed the 12.6 V charging threshold of a 12 V, 7 Ah SLA battery, delivering up to 25.92 W peak electrical power at 298.35 RPM and 0.1267 Ah of net charge per 5-minute trial at an overall system efficiency of 47.61 %. Post-trial open-circuit relaxation testing verified true electrochemical energy storage gains of up to + 0.011 V (≈ 0.92 % SoC) per 5-minute session alongside uninterrupted 5.0 V USB power regulation. Built at a total cost of ₦96,940, the system provides a durable, low-cost, and zero-emission auxiliary power platform suited for off-grid communities and instrumented exercise equipment.

DECLARATIONS

Funding: The authors declare that no external funding was received for this research.

Competing Interests: The authors declare that they have no competing or financial interests to disclose.

Availability of Data: The datasets generated and analyzed during the current study are available from the corresponding author upon reasonable request.

Ethical Approval and Consent to Participate: All experimental protocols involving human participants were conducted in accordance with institutional guidelines for non-invasive physical exercise testing, and informed consent was obtained from all 20 adult volunteers prior to participation.

Code Availability: The PIC16F877A embedded firmware code is available from the corresponding author upon reasonable request.

REFERENCES

1. Adewole, A. O., & Kiptoo, M. (2020). Energy poverty and decentralized renewable power generation in sub-Saharan Africa: A review of rural and peri-urban energy access models. *Journal of Cleaner Production*, 268, 122134. https://doi.org/10.1016/j.jclepro.2020.122134
2. Akinyele, D., Belikov, J., & Levron, Y. (2018). Battery storage technologies for electrical applications: Impact in stand-alone photovoltaic systems. *Energies*, 11(10), 2734. https://doi.org/10.3390/en11102734
3. Baker, N. J., & Spooner, E. (2002). Direct-drive permanent-magnet generators for small-scale renewable energy systems. *IEE Proceedings - Electric Power Applications*, 149(4), 249–256. https://doi.org/10.1049/ip-epa:20020489
4. Beretta, M., & Caputo, A. C. (2022). Design and experimental testing of a human-powered pedal generator for off-grid emergency charging applications. *Energy Reports*, 8, 4112–4124. https://doi.org/10.1016/j.egyr.2022.03.045
5. Bhattacharyya, S. C. (2012). Energy access problem of the poor: Opportunities and challenges for micro-grids in developing countries. *Energy Policy*, 42, 494–502. https://doi.org/10.1016/j.enpol.2011.12.014
6. Bhattacharyya, S. C., & Palit, D. (2016). Mini-grid based off-grid electrification to enhance electricity access in developing countries: What policies may be required? *Energy Policy*, 94, 166–178. https://doi.org/10.1016/j.enpol.2016.04.010
7. Chapman, S. J. (2012). *Electric machinery fundamentals* (5th ed.). McGraw-Hill Education.
8. Chen, Y., Pillay, P., & Khan, A. (2005). PM wind generator topologies. *IEEE Transactions on Industry Applications*, 41(6), 1619–1626. https://doi.org/10.1109/TIA.2005.858261
9. Chowdhury, S. A., & Razzak, M. A. (2019). Design and simulation of a low-speed hub alternator for stationary bicycle power generation. *IEEE Transactions on Energy Conversion*, 34(2), 890–898. https://doi.org/10.1109/TEC.2018.2882201
10. Deng, W., & Wang, Y. (2021). Recent advances in biomechanical energy harvesting: Mechanisms, materials, and applications. *Nano Energy*, 84, 105889. https://doi.org/10.1016/j.nanoen.2021.105889
11. El-Refaie, A. M. (2010). Fractional-slot concentrated-windings synchronous permanent magnet machines: Opportunities and challenges. *IEEE Transactions on Industrial Electronics*, 57(1), 107–121. https://doi.org/10.1109/TIE.2009.2030211
12. Gieras, J. F. (2010). *Permanent magnet electric machines: Design and applications* (2nd ed.). CRC Press.
13. Hanselman, D. C. (2006). *Brushless permanent magnet motor design* (2nd ed.). Magna Physics Publishing.
14. Hayt, W. H., Buck, J. A., & Akhtar, M. J. (2014). *Engineering electromagnetics* (8th ed.). McGraw-Hill Education.
15. Jansen, A. J., & Stevels, A. L. N. (2006). Combining eco-design and user benefits from human-powered energy systems, a win-win situation. *Journal of Cleaner Production*, 14(15–16), 1299–1306. https://doi.org/10.1016/j.jclepro.2005.11.023
16. Khaligh, A., & Onar, O. C. (2017). *Energy harvesting: Solar, wind, and energy harvesting modules*. CRC Press.
17. Kuang, Y., & Zhu, M. (2017). Characterisation of a knee-joint energy harvester powering a wireless communication sensing node. *Smart Materials and Structures*, 25(5), 055013. https://doi.org/10.1088/0964-1726/25/5/055013
18. Kwan, T. H., & Wu, X. (2016). Efficiency analysis and optimization of friction-driven vs. direct-drive biomechanical energy harvesters. *Applied Energy*, 179, 1188–1198.

https://doi.org/10.1016/j.apenergy.2016.07.086
19. Li, Z., & Chen, G. (2019). Design optimization of direct-drive permanent magnet synchronous generators for low-speed energy harvesting applications. *IET Electric Power Applications*, 13(7), 985–993. https://doi.org/10.1049/iet-epa.2018.5712
20. Lipo, T. A. (2017). *Introduction to AC machine design*. John Wiley & Sons.
21. Mazidi, M. A., McKinlay, R. D., & Causey, D. (2008). *PIC microcontroller and embedded systems: Using Assembly and C for PIC18*. Pearson Prentice Hall.
22. Mitcheson, P. D., Yeatman, E. M., Rao, G. K., Holmes, A. S., & Yeatman, T. (2008). Energy harvesting from human and machine motion for wireless electronic devices. *Proceedings of the IEEE*, 96(9), 1457–1486. https://doi.org/10.1109/JPROC.2008.927494
23. Mukherjee, S., & Mandal, N. (2020). Voltage multiplier-based low-voltage AC-DC power conditioning topologies for electromagnetic energy harvesters. *IEEE Transactions on Circuits and Systems II: Express Briefs*, 67(11), 2612–2616. https://doi.org/10.1109/TCSII.2020.2967412
24. Niu, S., Ho, S. L., & Fu, W. N. (2014). Performance analysis of a novel direct-drive permanent-magnet generator for human power harvesting. *IEEE Transactions on Magnetics*, 50(11), 1–4. https://doi.org/10.1109/TMAG.2014.2323214
25. Olabi, A. G., Wilberforce, T., Sayed, E. T., Elsaid, K., & Abdelkareem, M. A. (2021). Prospects of fuel cell and human-powered hybrid energy systems for off-grid applications. *Energy*, 226, 120351. https://doi.org/10.1016/j.energy.2021.120351
26. Parasuraman, S., & Elumalai, V. (2021). Performance characteristics of coreless permanent magnet axial flux generators for localized energy harvesting. *Journal of Electrical Engineering & Technology*, 16(4), 1985–1996. https://doi.org/10.1007/s42835-021-00720-z
27. Piller, S., Perrin, M., & Jossen, A. (2001). Methods for state-of-charge determination and their applications. *Journal of Power Sources*, 96(1), 113–120. https://doi.org/10.1016/S0378-7753(01)00560-2
28. Polinder, H., van der Pijl, F. F., de Vries, G. J., & Heck, M. B. (2006). Comparison of direct-drive and geared generator concepts for wind turbines. *IEEE Transactions on Energy Conversion*, 21(3), 725–733. https://doi.org/10.1109/TEC.2006.875476
29. Pyrhönen, J., Jokinen, T., & Hrabovcová, V. (2013). *Design of rotating electrical machines* (2nd ed.). John Wiley & Sons.
30. Rizzoli, G., Mengoni, M., Zarri, L., & Tani, A. (2022). Electromagnetic design and parasitic loss minimization in rim-mounted permanent magnet generators. *IEEE Access*, 10, 43102–43114. https://doi.org/10.1109/ACCESS.2022.3168901
31. Rubeis, T. D., Nardi, I., & Ambrosini, D. (2019). Off-grid human-powered systems: Empirical evaluation of pedal-generator power conversion efficiencies. *Energy Conversion and Management*, 196, 1245–1256. https://doi.org/10.1016/j.enconman.2019.06.071
32. Sadiku, M. N. O. (2018). *Elements of electromagnetics* (7th ed.). Oxford University Press.
33. Sahoo, S., & Dash, S. S. (2023). Design and performance evaluation of a multi-pole permanent magnet generator for low-RPM renewable and human-powered applications. *Electrical Engineering*, 105(3), 1543–1556. https://doi.org/10.1007/s00202-023-01748-1
34. Spooner, E., & Williamson, A. C. (1996). Direct-coupled, permanent-magnet generators for wind turbines. *IEE Proceedings - Electric Power Applications*, 143(1), 1–8. https://doi.org/10.1049/ip-epa:19960001
35. Starner, T. (1996). Human-powered computing. *IBM Systems Journal*, 35(3–4), 618–629. https://doi.org/10.1147/sj.353.0618

Tiwari, R., & Patel, V. (2018). Comparative performance analysis of mechanical drivetrain efficiency in bicycle power generation systems. *Renewable Energy Focus*, 26, 45–53. https://doi.org/10.1016/j.ref.2018.07.003

37. Valik, L., & Konecny, P. (2020). Embedded microcontroller-based real-time telemetry systems for decentralized renewable micro-generators. *Sensors*, 20(14), 3921. https://doi.org/10.3390/s20143921
38. Wang, C., & Zhang, J. (2015). Direct-drive biomechanical energy harvesting using high-grade NdFeB permanent magnet configurations. *Applied Physics Letters*, 107(12), 123902. https://doi.org/10.1063/1.4931702

39. Wang, J., & Howe, D. (2005). Design and optimization of permanent-magnet machines for direct-drive applications. *IEEE Transactions on Magnetics*, 41(10), 3922–3924. https://doi.org/10.1109/TMAG.2005.854964
40. Wong, K. C., & Chen, Y. S. (2021). Torque ripple reduction and flux enhancement in rim-integrated permanent magnet synchronous generators. *IET Electric Power Applications*, 15(5), 612–624. https://doi.org/10.1049/elp2.12051
41. Xu, D., & Zhu, Z. Q. (2017). Parametric analysis of cogging torque and back-EMF in permanent magnet machines with perimeter magnet arrangements. *IEEE Transactions on Magnetics*, 53(6), 1–9. https://doi.org/10.1109/TMAG.2017.2669112
42. Zhao, X., & Guerrier, P. (2018). Microcontroller-based charge controllers for battery storage in human-powered generator systems. *IEEE Transactions on Power Electronics*, 33(9), 7780–7791. https://doi.org/10.1109/TPEL.2017.2765410